


How to Quantify Heavy Mineral Fertility From Point-Counting Data

L. Stutenbecker¹ , D. Krieg², A. Djahansouzi², C. Glotzbach³, S. Falkowski^{3,4}, T. Adolffs⁵, S. Sindern⁵, and M. Hinderer²

¹University of Münster, Institute of Geology and Palaeontology, Münster, Germany, ²Technical University of Darmstadt, Institute of Applied Geosciences, Darmstadt, Germany, ³Department of Geosciences, University of Tübingen, Tübingen, Germany, ⁴University of Glasgow, School of Geographical & Earth Sciences, Glasgow, Scotland, UK, ⁵RWTH Aachen University, Institute of Applied Mineralogy and Economic Geology, Aachen, Germany

Special Collection:

Controls and Biasing Factors in Sediment Generation, Routing, and Provenance: Models, Methods, and Case Studies

Key Points:

- Relative mineral proportions in area percentage can be transformed to mass percentage using simplified grain shape and size metrics
- Mineral fertility can be estimated from detrital heavy mineral concentrates
- Results can be transformed to and compared with existing mineral fertility measurements

Correspondence to:

L. Stutenbecker,
laura.stutenbecker@uni-muenster.de

Citation:

Stutenbecker, L., Krieg, D., Djahansouzi, A., Glotzbach, C., Falkowski, S., Adolffs, T., et al. (2024). How to quantify heavy mineral fertility from point-counting data. *Journal of Geophysical Research: Earth Surface*, 129, e2023JF007545. <https://doi.org/10.1029/2023JF007545>

Received 17 NOV 2023

Accepted 11 APR 2024

Author Contributions:

Conceptualization: L. Stutenbecker, D. Krieg, C. Glotzbach
Data curation: L. Stutenbecker, D. Krieg
Formal analysis: L. Stutenbecker, D. Krieg, A. Djahansouzi, C. Glotzbach, T. Adolffs
Funding acquisition: L. Stutenbecker, C. Glotzbach
Investigation: L. Stutenbecker, D. Krieg, A. Djahansouzi, C. Glotzbach, T. Adolffs, S. Sindern
Methodology: L. Stutenbecker, D. Krieg, C. Glotzbach, S. Falkowski, T. Adolffs, S. Sindern
Project administration: L. Stutenbecker, C. Glotzbach, M. Hinderer
Resources: L. Stutenbecker, C. Glotzbach, T. Adolffs, S. Sindern, M. Hinderer

© 2024. The Authors.

This is an open access article under the terms of the [Creative Commons Attribution License](https://creativecommons.org/licenses/by/4.0/), which permits use, distribution and reproduction in any medium, provided the original work is properly cited.

Abstract Heavy minerals (HM) are widely used in provenance studies, for example, for reconstructing source areas and quantifying sediment budgets. Source rock mineral fertility influences the composition and concentration of HM in sediments. The resulting bias is of particular interest when interpreting single-grain data such as detrital age distributions. However, the quantification of fertility is complex and there are no robust data for most HM, which prevents the routine implementation of fertility in many studies. In this study, we test whether mineral fertility can be assessed by quantifying mineral concentrations in detrital samples through point counting and quantitative evaluation of minerals by scanning electron microscopy (QEMSCAN). The challenge is to transform the resulting area percentage into mass percentage, which is a prerequisite for comparing those data with grain size or geochemical data. We suggest overcoming this problem by recording grain-size and shape metrics of minerals using image analysis, and applying several transformation steps. We test our method by (a) using a series of detrital grain mixtures of known density and mass, and (b) applying it to a natural sediment from the European Alps. Our results agree with existing methods developed for apatite and zircon, that is, the quantification of fertility through geochemistry (with P₂O₅ and Zr concentrations as proxies for apatite and zircon) and the separation of pure apatite and zircon concentrates using additional separation steps. The advantage of our method is its applicability to all HM (not only apatite and zircon) and the redundancy of additional separation steps, which might create bias.

Plain Language Summary Heavy minerals (HM) are minerals of high density that usually occur in low percentages in most sediments and sedimentary rocks. The type and frequency of HM in sediments can help reconstruct the origin of the grains and thus sediment pathways on the Earth's surface. However, the absolute amount and relative proportions of HM can vary substantially, depending, for example, on the availability of these minerals in their source rocks (fertility). For studies that aim to quantify the amount of sediment supplied by different sources, the mineral fertility of all the sources in question should be known. However, such quantitative estimates are usually unavailable, and the existing methods to calculate fertility do not apply to a range of HM. We therefore suggest a procedure based on counting minerals under a microscope and transforming the resulting area percentage to mass percentage using grain-size and shape estimates. We test this procedure on artificial sediments with known grain proportions, sizes, and shapes and then apply it to natural samples. We show that using simple size and shape estimates, the resulting mass percentages are in accordance with published fertility data. We conclude that our method can be used to routinely estimate mineral fertilities quantitatively.

1. Introduction

Heavy minerals (HM) are widely used in provenance studies to reconstruct erosion, transport, and deposition in sediment routing systems (e.g., Caracciolo, 2020; Weltje & von Eynatten, 2004). HM contained in sediments or sedimentary rocks may, for example, provide information about the lithologies, metamorphic grades, and crystallization and cooling ages present in the source area (von Eynatten & Dunkl, 2012). Despite the rich information encrypted in heavy mineral grains, numerous processes can influence their occurrence and concentration, potentially leading to bias and erroneous interpretations in provenance studies (Garzanti & Andò, 2019). These processes include (a) varying heavy mineral concentrations in source rocks (fertility), leading to under- or overrepresentation of specific minerals in the detritus derived from certain lithologies

Supervision: L. Stutenbecker, C. Glotzbach, M. Hinderer
Validation: L. Stutenbecker, D. Krieg, A. Djahansouzi
Visualization: L. Stutenbecker, D. Krieg
Writing – original draft: L. Stutenbecker, D. Krieg
Writing – review & editing: L. Stutenbecker, D. Krieg, A. Djahansouzi, C. Glotzbach, S. Falkowski, T. Adolffs, S. Sindern, M. Hinderer

(e.g., Moecher & Samson, 2006), (b) hydraulic sorting and selective entrainment that may lead to the enrichment or depletion of minerals of certain densities, sizes or shapes (e.g., Garzanti et al., 2008; Komar, 2007), and (c) weathering or diagenetic effects that may deplete or eliminate less stable mineral species (e.g., Morton & Hallsworth, 1999).

Although fertility-related bias is widely recognized (Chew et al., 2020; Dickinson, 2008; Malusà et al., 2016), mineral fertility is not easily quantified, and fertility data are scarce and therefore challenging to implement routinely in provenance studies. Dickinson (2008) addressed zircon fertility by analyzing zirconium (Zr) contents using bulk rock geochemistry and concluded that zircon fertility varies by a factor of 5 even in similar (in this case, granitic) lithologies. Therefore, quantifying fertility by directly analyzing the heavy mineral contents in source rocks would require extremely dense sampling of all potential source rocks. Especially in large catchments with multiple source lithologies, this is often not feasible due to financial and temporal constraints. Malusà et al. (2016) suggested that the heavy mineral content of detrital fluvial sediment produced in proximal catchments mirrors source rock fertility if the heavy mineral spectrum is not modified during transport or deposition. These authors compared sediment geochemistry (with P_2O_5 and Zr contents as proxies for apatite and zircon, respectively) with the mass of apatite and zircon grains separated from the bulk sediment through magnetic, hydraulic, and heavy liquid mineral separation techniques. They concluded that the geochemistry approach consistently overestimates the actual apatite and zircon concentrations. This can be explained by other minerals incorporating Zr and P_2O_5 and/or zircon and apatite occurring as small inclusions detected by geochemistry but not separated using mineral separation approaches. Both the “geochemistry approach” (sensu Dickinson, 2008) and the “separation approach” (sensu Malusà et al., 2016), however, have limits for routine fertility estimation. Firstly, the separation approach favors grains that behave similarly in the different separation steps. However, detrital grains from the same mineral species may behave differently during (a) hydraulic separation using shaking tables due to different grain sizes (Sláma & Košler, 2012) or grain shapes (e.g., rounded vs. prismatic/elongated grains), (b) magnetic separation due to different magnetic properties (Heaman & Parrish, 1991; Sircombe & Stern, 2002), and (c) heavy liquid separation due to intergrowth with other, lighter or heavier, phases. Secondly, both the geochemistry and separation approaches are not applicable to most other HM because they (a) exhibit larger geochemical variability than zircon and apatite (e.g., the tourmaline or garnet groups), (b) lack a clear geochemical proxy (e.g., the TiO_2 minerals, as Ti also occurs in other dense phases such as titanite and ilmenite), and (c) cannot be separated from other HM through mineral separation techniques because of similar shape, density or magnetic properties. This limited applicability of the existing fertility measures is problematic because other (heavy) minerals are increasingly used in quantitative provenance analysis, for example, for mixing modeling and sediment budgeting (e.g., mica in Gemignani et al., 2017; K-feldspar in Zhang et al., 2014; amphibole in Vezzoli et al., 2016).

In this paper, we explore the quantification of fertility based on the mineral distribution in detrital samples without further separation. We determined the area percentage of different minerals via point counting, image analysis, and automated mineral analysis using QEMSCAN. Although such area percentage data are often collected in heavy mineral studies, the conversion from area percentage to mass percentage needed to quantify fertility is complex. We test the conversion using a series of grain mixtures with known mass and density and record grain shapes and sizes while point counting and via image analysis. Furthermore, we apply the conversion steps to a natural river sand sample from the European Alps and test if the calculated heavy mineral mass percentages match the expected mineral fertility. The data are then compared to the separation and geochemistry approaches of Malusà et al. (2016) and Dickinson (2008) for apatite and zircon.

2. Experimental Setup and Methods

2.1. Converting Area Percentage to Mass Percentage

Heavy mineral concentrates are usually embedded in resins to produce grain mounts, thin sections, or strewn slides (Andò, 2020). Point-counting is a standard method to quantify the relative proportions of different mineral species (Galehouse, 1971). Point-counting using the Glagolev-Chayes method provides area percentage (area%) because the probability of a grain being hit by the point-counting grid is proportional to its area in the thin section (Chayes, 1954). Traditional heavy mineral counting often uses the Fleet, ribbon, or line methods instead, which provide number percentages (Galehouse, 1971). To calculate the concentration of HM in the bulk sediment, however, two key figures are needed that are usually provided in mass percentage (mass%). Firstly, due to their

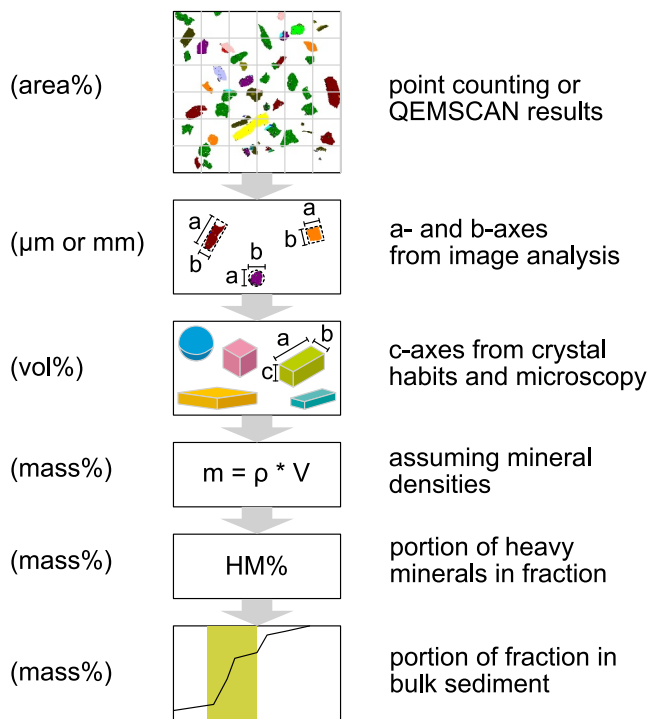


Figure 1. Proposed steps in converting mass percentage (mass%) from point-counting results (area%). With m : mass, ρ : density, V : volume, HM: heavy minerals.

higher density and the resulting size shift with respect to the less dense framework grains (Garzanti et al., 2008), HM tend to be enriched in the finer tail of the sediment. Accordingly, most researchers extract HM from one or several grain-size fractions ranging from medium and fine sand to silt (Garzanti & Andò, 2019). The proportion of the used grain-size fraction from the bulk sediment is usually quantified by sieving the sediment and weighing each grain-size fraction, which provides the mass percentage. Secondly, HM are typically separated from less dense grains using gravimetric separation techniques (Andò, 2020). The separated “light” (less dense) and “heavy” (dense) fractions are then weighed to calculate the heavy mineral concentration in the sample in mass percent (Garzanti & Andò, 2007). Given these different units, converting the point-counting results (in area or number percentage) to mass percentage seems preferable. Area percentage may be assumed to be equivalent to volume percentage (vol%) in rock-thin sections where mineral axes are cut randomly (Chayes, 1954). However, samples used for heavy mineral counting are usually produced from loose material, and grains tend to fall on their shortest grain axis (termed c-axis from here on) during the embedding process. Grains with a very short c-axis compared to their a- and b-axis (i.e., platy grains such as mica) may therefore have a considerably higher area percentage than volume percentage compared to isometric or prismatic grains. Thus, additional grain size and shape information is needed to convert area percentage to volume percentage, which must be determined individually for each sample. After compiling such information (Section 2.5), we convert volume percentage to mass percentage using heavy mineral densities compiled by Resentini et al. (2013). The concentration of each heavy mineral (now in mass percentage) in the bulk sediment (Figure 1) is calculated by multiplying with the heavy mineral

concentration (in mass percentage) and the fraction of the used grain size window from the bulk sediment (in mass percentage from sieving).

2.2. Samples and Sample Preparation

We tested the proposed method by creating a series of artificial sediments from detrital mineral species of known size, shape, and density. The first series consisted of a three-component sand produced from magnetite, blue-colored quartz, and red-colored quartz grains. The quartz was produced from commercially available natural quartz sand (>90% SiO₂) that was further purified using magnetic separation at 1.8 A. The non-magnetic fraction was split into two fractions, and these were dyed with commercially available acrylic blue and red paint. After air-drying for 2 days, the quartz was dry-sieved to 125–250 μm. The magnetite portion was produced from an almost pure (~99%) magnetite placer deposit from Klima beach (Milos, Greece) that was further purified using a hand magnet and then sieved to 63–125 μm to simulate the natural size shift between quartz and magnetite (Garzanti et al., 2009; Resentini et al., 2013). All grains had similar, rounded, and slightly irregular shapes. The magnetite and blue and red quartz were then mixed to achieve mass proportions of approximately 50, 10, 5, and 1 mass% magnetite (Table 1) by weighing the grains with a high-precision scale. The second artificial sample was produced from biotite and the same red quartz described above. The biotite was separated from beach sand collected at

Table 1
Weighted Proportions of Red Quartz, Blue Quartz, and Magnetite for the Four Artificial Sand Samples

Magnetite to quartz ratio	Red quartz		Blue quartz		Magnetite	
	[g]	[Mass%]	[g]	[Mass%]	[g]	[Mass%]
~50:50	0.0112	24.30	0.0119	25.81	0.0230	49.89
~10:90	0.0503	79.84	0.0064	10.16	0.0063	10.00
~5:95	0.0505	90.50	0.0025	4.48	0.0028	5.02
~1:99	0.0674	97.26	0.0012	1.73	0.0007	1.01

Platja Sant Pol (Catalonian mountain range, NW Spain) using gravimetric separation (Andò, 2020) of the 250–500 μm grain-size fraction. The resulting heavy mineral concentrate consisted almost entirely of biotite ($\sim 95\%$), and the few other grains were removed by hand-picking under a microscope. Grains were mixed to a proportion of 10 mass% biotite and 90 mass% red quartz using a high-precision scale.

The artificial grain mixtures were shaken thoroughly, and all grains were poured onto glass slides with Canada balsam to prepare strewn slides. The strewn slides were not ground or polished. From all artificial mixtures, high-resolution scans were obtained using a Keyence VHX 7000 digital microscope at the University of Münster. The initial mass of mineral fractions can not only be expressed in terms of mass% but also in vol% using calculated densities based on molecular masses and volumes (via webmineral.com; we used 2.65 g/cm^3 for quartz, 5.2 g/cm^3 for magnetite, and 2.9 g/cm^3 for biotite).

Furthermore, we used one natural river sediment collected along a sand bar of the river Ziller in the Austrian Alps. At the sampling site (N 47.158026, E 11.876757), the Ziller drains a $\sim 160\text{-km}^2$ -large catchment predominantly ($>80\%$) composed of the “Zentralgneis” (=central gneiss) of the Tauern window (Schmid et al., 2004). The Zentralgneis was formed by Paleogene amphibolite-facies metamorphism that overprinted Permo-Carboniferous plutonic bodies of granitic to tonalitic composition (Bousquet et al., 2012; Lammerer & Weger, 1998). Inter-calated are minor occurrences of basic (meta-)volcanic rock, amphibolite, metasedimentary rock, and carbonate (GBA, 2015).

The Ziller sand sample was sieved into individual grain-size fractions (<63 , 63–125, 125–250, 250–500, 500–1,000, 1,000–2,000 μm). The material of each size window was dried and weighed. HM were separated using gravimetric separation of the 63–125, 125–250, and 250–500 μm fractions. First, a representative aliquot was obtained using a riffle box. The samples were then separated using sodium polytungstate at a 2.9 g/cm^3 density in separation funnels. The obtained heavy mineral concentrates were rinsed with water, dried, and weighed. We calculated the heavy mineral concentration by dividing the mass of the heavy mineral concentrate by the total sample mass before separation (HM% after Garzanti & Andò, 2007). Split fractions of the concentrates were mounted on double-sided sticky tape and embedded in epoxy resin to produce grain mounts. The grain mounts were subsequently ground and polished to expose the contained grains.

2.3. Accounting for Selective Entrainment

Selective entrainment processes may influence the absolute concentration of HM in a natural river sediment (Garzanti et al., 2008, 2009; Komar, 2007). Less dense minerals like quartz and feldspar tend to be larger than the HM they were deposited with (settling-equivalence principle, Garzanti et al., 2008; Rubey, 1933). Larger, less dense minerals are, in turn, easier to be entrained by the current (Komar, 2007; Komar & Li, 1988), which can lead to the enrichment of HM and eventually to the formation of placer deposits (Reid & Frostick, 1985). For the heavy mineral concentration to faithfully reflect source rock fertility, selective entrainment processes should either be absent or corrected (Malusà et al., 2016). Bulk densities for modern sediments commonly range between 2.65 and 2.8 g/cm^3 (Garzanti & Andò, 2007), depending on the provenance and selective entrainment, which can lead to notably higher values. Garzanti et al. (2012) suggested identifying samples affected by selective entrainment by measuring the bulk sediment density using a hydrostatic balance. However, the method is time-consuming and prone to erroneous results due to the incomplete elimination of interstitial air (Garzanti et al., 2012). Therefore, we used a Micromeritics® helium pycnometer which yields quicker and more reproducible results. 30 g of the sample material was filled in a chamber of known volume and placed in the gas pycnometer. The pycnometer introduces a known volume of gas into the chamber and measures the pressure building up. The pressure is released by letting the gas flow into an expansion chamber of known volume. The sample volume is calculated using the difference between the known volume of the chamber and the expansion chamber divided by the pressure measurements. The density of the sample material is then calculated by dividing the sample mass by the sample volume attained by the pycnometer. Given the axial belt provenance of the Ziller, we assumed a density between 2.7 and 2.8 g/cm^3 for the Ziller sand (Garzanti & Andò, 2007; Garzanti et al., 2010; Malusà et al., 2016). Lower or higher values suggest hydraulic sorting bias. Finally, the composition of the Ziller sample was compared with available geochemical and mineralogical compositions of its main source rock, the Zentralgneis of the Tauern window (Finger et al., 1993; Melcher et al., 1996; Raith, 1970; Wyss, 1993) to evaluate if the sand composition deviates from the source rock composition.

2.4. QEMSCAN Analysis

Point-counting results may be biased by operator experience (Dunkl et al., 2020) and may have relatively high uncertainties depending on the number of total counts and the percentage of the mineral in question (van der Plas & Tobi, 1965). Therefore, we analyzed the heavy mineral spectra of the Ziller sediment using QEMSCAN, which analyses more grains per sample and generally has higher analytical accuracy than manual point-counting (Dunkl et al., 2020). A Quanta 650-F QEMSCAN© (FEI/Thermo Fisher) scanning electron microscope (SEM) was used at the Institute of Applied Mineralogy and Economic Geology, RWTH-Aachen University. The polished epoxy mounts bearing the sample material (fractions 250–500 μm , 125–250 μm , and 63–125 μm) were analyzed after carbon coating. The SEM measurements were performed with an acceleration voltage of 15 kV and a fixed sample current of 10 nA while operating in particle mineralogical analysis mode (PMA mode). In contrast to the field scan mode which is used for the measurement of non-particulate samples, the PMA mode is used for measuring samples containing individual particles. Prior to the measurement itself, the QEMSCAN system automatically identifies particles and their extents. Conducting the measurement in PMA mode then produces an individual image and corresponding spectral data for each particle. The spatial surface resolution of the measurement was set to 5 μm . The backscattered electron (BSE) intensities for each 5×5 - μm pixel were recorded with a 4-quadrant BSE detector, while the individual X-ray spectra were recorded with two DualXFlash 5030 SDD energy dispersive x-ray detectors manufactured by Bruker AXS (Karlsruhe, Germany). The mineral phases were identified by comparing measured spectral data for each 5×5 - μm pixel with library data. The library data were provided by the SEM device-specific iDiscover software suite (Version 5.3.2.501, FEI/Thermo Fisher, Hillsboro, OR, USA). The identification of the mineral phases was then carried out after a comparison of the measured spectra with the mineral phases listed in a species identification protocol created by the operator. Mineral phase identification follows a first-match and best-fit procedure. After the mineral phase identification, images of the sample material were created, and each sample's modal composition in area percentage was calculated. In addition, the QEMSCAN software calculates mineral associations by identifying all neighboring pixels to each pixel. Minerals that are predominantly associated with “background” pixels (i.e., epoxy resin) or unidentified, “low-confidence” pixels (that occur frequently along cracks or on the rim due to poor and/or mixed BSE signal) can be assumed to occur as individual particles, whereas minerals associated with other minerals occur either in polymineralic grains or as inclusions.

2.5. Grain-Size and Shape Metrics

Both the Ziller sample QEMSCAN phase maps and the artificial sand scans were analyzed with the Fiji derivation of ImageJ (Schindelin et al., 2012; Schneider et al., 2012) to describe and quantify grain shapes and sizes. Each grain was defined by the operator instead of using a grain-separation algorithm, because the algorithms were unable to separate touching or overlapping grains, mis-identified air bubbles as grains in the artificial samples, and did not perform well with composite grains in the Ziller sample. Composite grains in the Ziller sample were considered as individual minerals only if they were mostly monomineralic, that is, consisting of over 80 area% of one single mineral phase (Figure 2a; not including unidentified pixels, which are often found on the grain rims or along cracks). Composite grains consisting of two or more individual, clearly separated minerals larger than 40 μm were counted as individual phases (Figure 2b), whereas composite grains consisting of multiple smaller or strongly intergrown phases were treated as rock fragments (Figure 2c).

We measured the longest and shortest visible axes, which we term “a-axis” and “b-axis,” respectively, from here on, of all defined individual grains in the samples. In order to calculate the area of each grain using the grain diameters, the shape of the particles has to be approximated. Because all grains in the artificial samples have the same shapes, we assumed simple circular shapes for quartz and magnetite. In contrast, the Ziller sample consists of a range of minerals with different shapes, and we tested the best-fitting area approximation by comparing the true and calculated areas of selected grains. We measured the a- and b-axes of 160 mostly monomineralic, differently shaped grains of apatite, biotite, epidote, feldspar, garnet, hematite, hornblende, ilmenite, pyrite, titanite and zircon and calculated their areas using circles, squares, ellipses and rectangles. The same grains were measured using the wand-tool in ImageJ, which selects all pixels of the same color within a grain and calculates their true area. The best fit between calculated and true area was determined using the least square method (Stutenbecker, 2024a), and we accordingly assumed elliptic shapes for all grains except for the phyllosilicates, which were best approximated using rectangular shapes:

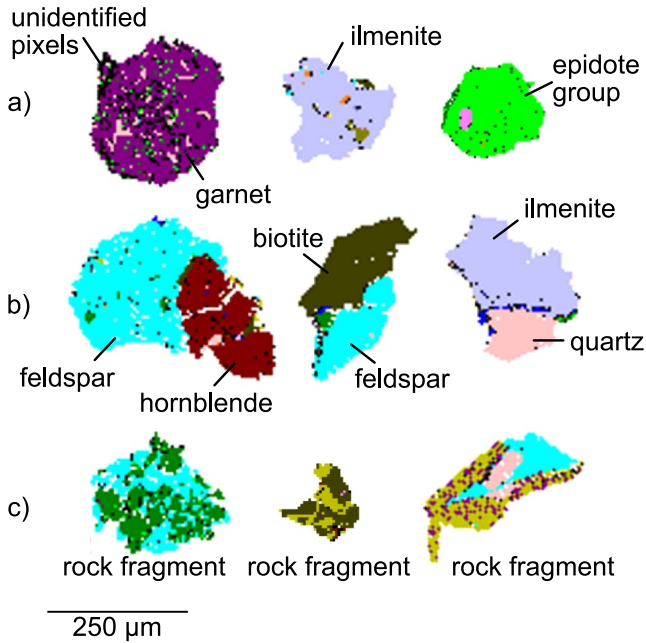


Figure 2. Composite grains in the Ziller samples were considered individual grains only if they were largely monomineralic (>80%, not counting unidentified pixels often found along the grain rims) (a), or, if polycrystalline, if the individual grains were larger than 40 μm (b). Composite fragments consisting of smaller intergrown phases (c) were treated as rock fragments.

$$A_{\text{rectangle}} = a * b \text{ for the phyllosilicates,} \quad (1)$$

where a = diameter of a-axis, b = diameter of b-axis.

$$A_{\text{ellipse}} = \pi * a/2 * b/2 \text{ for all other grains,} \quad (2)$$

where a = diameter of a-axis, b = diameter of b-axis.

The (presumably shortest) axis that is not visible in the two-dimensional maps or scans, the “c-axis,” was examined and measured by turning >20 loose grains of the most abundant and easily identifiable mineral species (apatite, biotite, epidote group, garnet, hornblende, zircon) of the 63–125 and 125–250 μm fractions under a Keyence VHX 7000 digital microscope. Both the b-axis and the c-axis of a total of 158 grains were measured. The mean b-to-c-axis ratio of each mineral group was subsequently used to calculate the c-axis of all grains in the sample using the b-axis measured from the 2D phase maps. If the b-to c-axis ratio was not quantifiable (e.g., because the mineral had low abundance or was not identifiable in a reliable way under transmitted light), we made b-to c-axis ratio assumptions based on microscope observations and typical crystal shapes. For white mica and chlorite, we assumed the same ratios as for biotite. For ankerite, pyrite, quartz-feldspar rock fragments and the TiO₂ phase, we assumed a c-axis equal to the b-axis. For ilmenite, hematite, and titanite, we assumed the same ratio as for epidote. Based on the (detrital) crystal shapes observed during microscopy, we then calculated the volume of all grains as follows:

$$V_{\text{rectangle}} = a * b * c \text{ for the phyllosilicates,} \quad (3)$$

where a = diameter of a-axis, b = diameter of b-axis, c = diameter of c-axis.

$$V_{\text{ellipse}} = 4/3 * \pi * a/2 * b/2 * c/2 \text{ for apatite, garnet, monazite, the TiO}_2 \text{ phase and zircon,} \quad (4)$$

where a = diameter of a-axis, b = diameter of b-axis, c = diameter of c-axis.

$$V_{\text{cylinder}} = \pi * a/2 * b/2 * c \text{ for ankerite, the epidote group minerals, hornblende, the opaque phases, titanite, and quartz – feldspar rock fragments,} \quad (5)$$

where a = diameter of a-axis, b = diameter of b-axis, c = diameter of c-axis.

Because the Ziller samples were prepared as polished grain mounts for QEMSCAN analysis (Section 2.2), the grain diameter measured in 2D phase maps is an apparent one and not the true diameter. Due to the range of grain sizes within a sieved fraction, grains may be cut at a random diameter that is not necessarily equal to but potentially smaller than their true (equatorial) diameter. The mismatch between measured (apparent) and true diameter is larger for large grains than for small grains and pronounced for spherical and ellipsoid grains, whereas it is absent for cubic and cuboid grains (Figure 3a). This effect is negligible for samples prepared as strewn slides because the entire area of a grain is usually visible under transmitted light, even if a large proportion of the grain is below the surface of the strewn slide. Natural samples usually contain a range of grain sizes and shapes. If they are prepared as polished grain mounts, a correction procedure is therefore necessary (Figure 3b). If the thickness of the material h that is removed by grinding and polishing (i.e., the difference between the original surface S_O and the exposed surface S_E) is known or can be estimated in a reliable way, and the apparent diameter D_m is measured, the true diameter D_t can be calculated as the chord length for spheric or ellipsoid grains as follows:

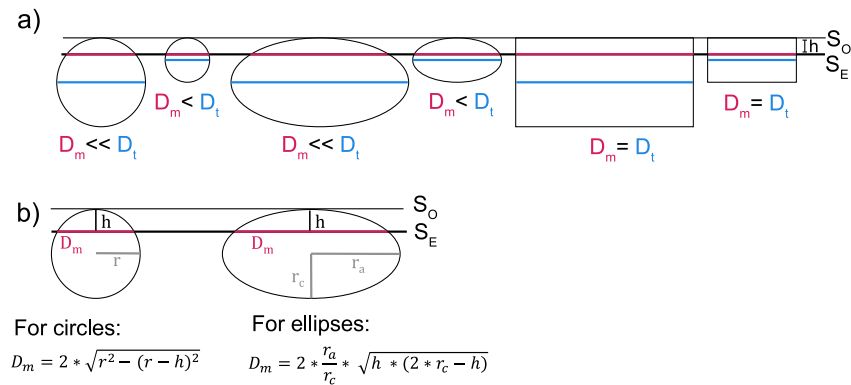


Figure 3. (a) Measured (apparent) diameter, D_m , vs. true diameter, D_t , of spheric, ellipsoid and cuboid grains of different sizes if prepared as polished grain mounts. In this sample preparation technique, the original surface S_O is ground down to an exposed surface S_E by an amount h . (b) Chord lengths for spheric and ellipsoid grains with r = radius, r_a = radius of a-axis, r_c = radius of c-axis.

$$D_t = 2 * \frac{D_m^2 + 4 * h^2}{8 * h} \text{ for spheres, and} \quad (6)$$

$$D_{l(a)} = 2 * \left(\frac{D_{m(a)}^2 * x}{8 * h} + \frac{h}{2x} \right) \text{ for ellipsoids, with } x = c/a \quad (7)$$

The thickness h can be determined by placing a few commercially available glass beads of known diameter on the sticky tape along with the sample material before casting the epoxy resin, measuring their diameter after grinding and polishing and applying Equation 6. In the case of ellipsoid grains, the ratio between the a-axis and b-axis does not change due to grinding the sample by a thickness h . Therefore, the diameter of the true a-axis $D_{l(a)}$ calculated through Equation 7 can be used to calculate the true b-axis based on the known ratio of the apparent a-axis and b-axis. The ratio of a-axis to c-axis, however, changes due to the grinding process. In our case, this correction process works anyway because we can assume that the c-axis is roughly equal to the b-axis for ellipsoid grains such as apatite, garnet, and zircon (see Section 3.2).

2.6. Point Counting

The artificial sand samples were point-counted using the Glogolev-Chayes method to obtain area percentage values (Chayes, 1954). The samples were counted three times each with at least 200 counts each time. The uncertainty of point-counting results depends on the overall number of grains counted and the proportion of the counted phase, where phases with low proportions have higher uncertainty than phases with high proportions (van der Plas & Tobi, 1965). We estimated the uncertainty of the point-counting results applying the method proposed by van der Plas and Tobi (1965) using the standard deviation.

2.7. Image Analysis Using a Color Threshold

The artificial grain mixture scans were processed in ImageJ to obtain an additional estimate for area percentage. Because of the simple and homogenous grain colors, we used the “color deconvolution” tool to define and split the colors (red, blue, and black for the quartz/magnetite mixtures; red and dark brown for the quartz/biotite mixture). Afterward, the “color threshold” and “analyze particles” tools were used to transform all red, blue, black, and brown pixels into separate black-and-white grain maps and measure each grain’s area (Figure 4). The resulting pixel count for each color class was divided by the total pixel count to get area%. Furthermore, image data allowed total grain counting and determination of grain or number% values (i.e., Fleet method).

2.8. Separation Approach

From the Ziller sample, apatite and zircon grains were separated using established mineral separation protocols at the University of Tübingen that are similar to those reported by Malusà et al. (2016). We used MinSorting

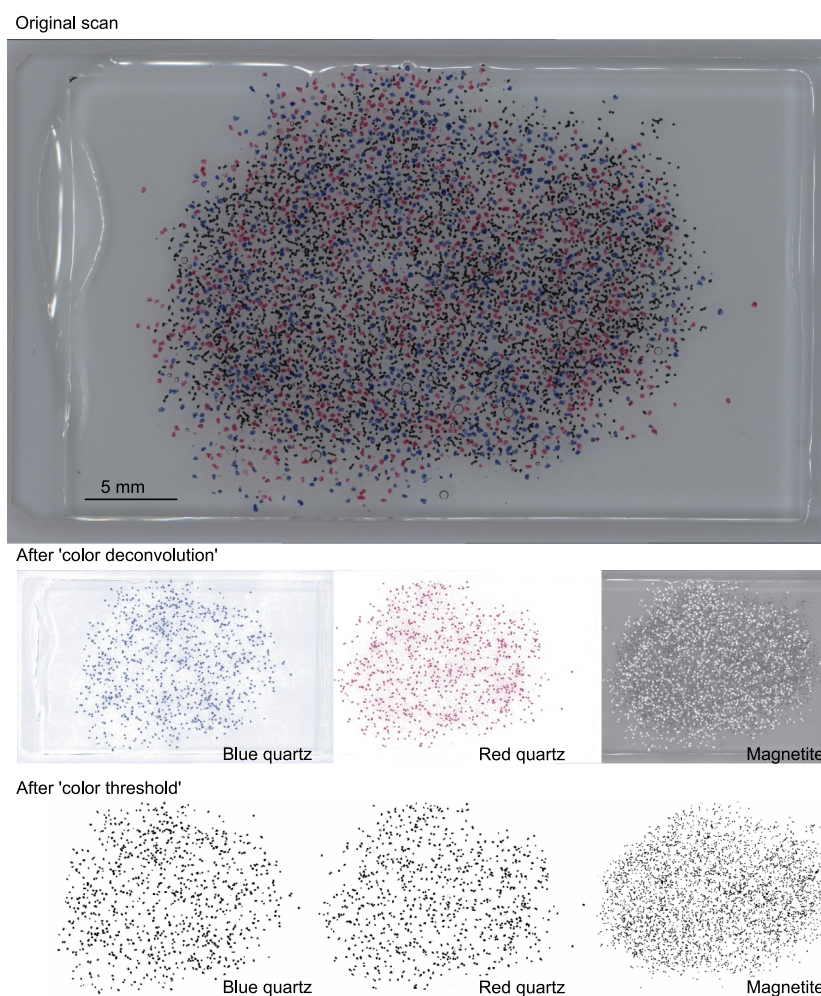


Figure 4. Example image analysis of the artificial grain mixtures (here, the 50 mass% magnetite sample). First, the three colors are split into three separate channels and then processed using a color threshold that transforms the image into simple black-and-white grain maps, which can then be analyzed using the “analyze particles” tool of ImageJ.

(Resentini et al., 2013) to identify the grain-size fractions that should contain most apatite and zircon according to the expected size shift of these minerals. The grain size fractions of 63–125 μm , 125–250 μm , 250–500 μm , and 500–1,000 μm were separated using magnetic separation at 1.75 A. The non-magnetic fractions expected to host most of the apatite and zircon grains were separated twice using sodium polytungstate (at 2.8 g/cm^3) and methylene iodide (at 3.32 g/cm^3). Apatite (density of ca. 3.2 g/cm^3) should be contained in the concentrate between 2.8 g/cm^3 and 3.32 g/cm^3 , whereas zircon (density of ca. 4.65 g/cm^3) was expected in the concentrate $>3.32 \text{ g}/\text{cm}^3$. However, the produced concentrates were rarely entirely pure, so the content of the two targeted minerals was determined by point counting of the individual separates (Malusà et al., 2016).

2.9. Geochemistry

The concentrations of phosphorus oxide (P_2O_5) and zirconium (Zr) may be used as proxies for apatite and zircon concentrations, respectively (Dickinson, 2008; Malusà et al., 2016). Accordingly, we measured P_2O_5 and Zr concentrations within the narrow grain size fractions and the bulk sample of the Ziller sediment. The samples were milled in an agate jar at 750 cycles per second for 2 minutes. The major element oxides and a suite of common trace elements, including Zr, were analyzed via lithium borate fusion coupled with ICP-MS at Bureau Veritas ACME laboratories in Vancouver, Canada. The detection limits for P_2O_5 and Zr were 0.01 wt% and 5 ppm, respectively. We applied atomic/molecular mass factors to account for the amount of P_2O_5 in apatite ($\text{Ca}_5(\text{PO}_4)_3\text{F}$, factor 0.454) and the amount of Zr in zircon (ZrSiO_4 , factor 0.497). To account for the complex

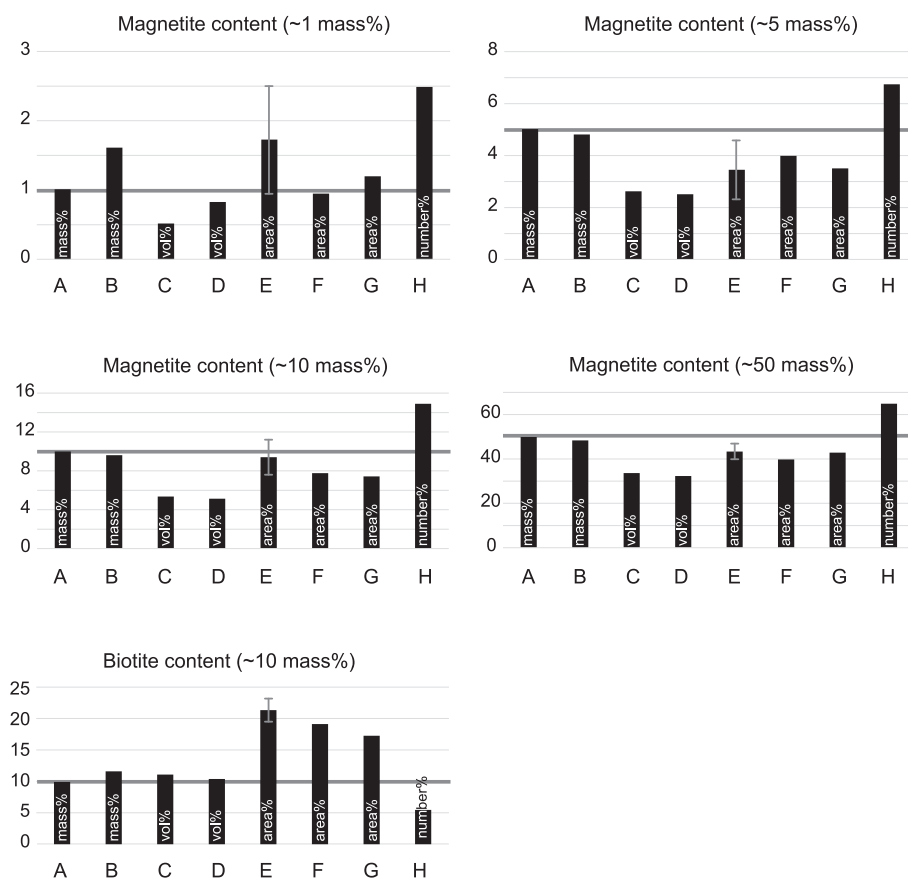


Figure 5. Comparison of magnetite contents of the four artificial quartz-magnetite sands and the biotite content in the quartz-biotite sample in mass%, vol%, area%, and number%. (a) Initial (weighted) mass% based on the mass of magnetite, quartz, and biotite grains. See Table 1 for data. (b) Mass% calculated based on grain radii measured by image analysis and approximated mineral shapes. See Stutenbecker (2024b). (c) Initial vol%: calculated based on the initial weighted mineral proportions (a) and literature values of molecular masses and volumes. (d) Vol% calculated based on grain radii from image analysis (b) and c-axis values. (e) Area% determined by point-counting using the Glagolev-Chayes method; the uncertainty of the point-counting results (error bar) was calculated following van der Plas and Tobi (1965). See Stutenbecker (2024c) for data. (f) Area% calculated based on grain radii from image analysis (b) and b-axis values. (g) Area% of values extracted from color-deconvoluted high-resolution scans (image analysis). See Stutenbecker (2024d) for data. (h) Number% obtained after grain counting in image data. See Stutenbecker (2024b) for data.

character of the multielement data set, and to visualize, characterize, and compare the results with literature data, concentration values were log-ratio transformed and further processed by principal component analysis. For multivariate data analysis, we used the software package CoDaPack (Thió-Henestrosa & Martín-Fernandez, 2006).

3. Results

3.1. Artificial Grain Mixtures

The measurements of the a- and b-axes (Stutenbecker, 2024b) of all grains via image analysis provide mean grain sizes for magnetite (a: 168 μm , b: 117 μm), red quartz (a: 235 μm , b: 170 μm), blue quartz (a: 263 μm , b: 186 μm), and biotite (a: 512 μm , b: 348 μm). Based on the microscope observations, the quartz and magnetite grains were assumed to have c-axis similar to their b-axis. In contrast, we measured a mean c-axis of 90 μm ($\pm 12 \mu\text{m}$) based on 30 individual grains for the platy biotite. Overall, the area percentages derived through (a) point-counting, (b) image analysis using a color threshold, and (c) grain-size analysis (calculating areas using mean b-axis as sphere radii) yield identical results within the error of manual point-counting (Figure 5, see Stutenbecker, 2024b, 2024c, 2024d). The largest deviation occurs for the 1 mass% magnetite sample, where the magnetite area percentage

Table 2

Grain-Size Distribution, Sediment Density, Heavy Mineral Concentration, and MinSorting-Modeled Apatite and Zircon Percentages of the Ziller Sand (Sample Site N 47.158026, E 11.876757)

Grain-size fraction	Mass of fraction after sieving (mass%)	Density (g/cm ³)	Heavy mineral concentration (mass%)	Expected percentage of apatite contained in fraction (MinSorting)	Expected percentage of zircon contained in fraction (MinSorting)
Bulk	99.72 (loss of 0.28)	2.725	Not determined	100	100
1,000–2,000 μm	9	2.693	Not determined	6.0	2.2
500–1,000 μm	27.14	2.705	2.43	20.6	12.4
250–500 μm	33.65	2.706	1.33	33.9	31.0
125–250 μm	19.92	2.726	7.32	26.7	34.1
63–125 μm	7.48	2.732	3.46	10.1	16.5
<63 μm	2.53	2.776	Not determined	1.9	3.6

Note. Note that the MinSorting model assumes that all mineral species may be present in each grain size fraction.

derived from point counting is almost twice as high as the value derived from image analysis. When converting area percentages to volume percentage (using the assumed/measured c-axis values) and finally to mass percentage (using density estimates), the result falls within 95% of the initial mass percentage determined by high-precision weighing (Figure 5). Number and mass percentages are considerably higher than area percentage, and area percentage is higher than volume percentage for all magnetite-quartz mixtures. In the case of biotite, the volume percentage is similar to the mass percentage, the area percentage is considerably higher, and the number percentage is lower than the mass percentage.

3.2. Ziller Sample

The Ziller sample is a unimodal sand with a mean grain size of 365 μm (M_G ; Folk & Ward, 1957) and poor sorting (σ_G of 2.24, Folk & Ward, 1957). Its bulk sediment density is 2.725 g/cm³, with the highest density measured in the finest fraction (<63 μm: 2.776 g/cm³) and the lowest density in the coarsest fraction (1,000–2,000 μm: 2.693 g/cm³). According to MinSorting modeling, 71% of apatite and 82% of zircon should be contained in the 63–500 μm fraction, but significant amounts should also be present in the 500–1,000 μm fraction (Table 2).

Heavy mineral concentrations in the Ziller fractions are between 1 and 7 mass% (Table 2). The heavy mineral spectra of the Ziller sediment obtained by QEMSCAN analysis (Figure 6; Stutenbecker, 2024e) are dominated by epidote group minerals (15–37 area%), phyllosilicates (13–38 area%, dominantly biotite with minor chlorite and muscovite), and amphibole (14–17 area%, dominantly blue-green hornblende). Quartz (2–8 area%) and feldspar (2–8 area%, dominantly plagioclase) are often associated with amphiboles or biotite in rock fragments. Other phases are garnet (4%–8%), apatite (2–6 area%), ilmenite (1–4 area%), hematite (1–3 area%), titanite (1–2 area%), and ankerite (0.4–2 area%). Phases with concentrations below 1% include pyrite (0.5–1 area%), zircon (0.02–1 area%), TiO₂ phases (0.1–0.6 area%), and monazite (0.02–0.5 area%). The contents of ankerite, biotite, feldspar, quartz, and TiO₂ phases decrease with decreasing grain size, whereas the contents of apatite, epidote, muscovite, and zircon increase with decreasing grain size. Other minerals show no clear grain-size-dependent trend (chlorite, garnet, hematite, ilmenite, pyrite, and titanite). Hornblende has overall similar proportions in all grain size fractions.

In the 63–125 μm fraction, 86.3% of apatite and 65.4% of zircon are associated with background or low-confidence pixels, that is, they occur as individual apatite or zircon grains (Figure 7). This proportion decreases in the 125–250 μm fraction (apatite: 66.1%, zircon 18.9%) and even further in the 250–500 μm fraction (apatite: 29.5%, zircon: 0%). For all other mineral associations, the reader is referred to Stutenbecker (2024e).

Mean grain sizes were measured via image analysis within the 63–125 and 125–250 μm fractions (Figure 8) because the coarser grain-size fractions comprise mainly phyllosilicates and complex composite grains rather than individual minerals. The raw data can be found in Stutenbecker (2024f). Mean grain axes were 196 ± 64 μm for the a-axis and 120 ± 39 μm for the b-axis in the 125–250 μm fraction, and 111 ± 12 μm (a-axis) and 61 ± 4 μm (b-axis) in the 63–125 μm fraction. Overall, the range of grain sizes, expressed as the relative standard deviation, was considerably smaller (11% and 6% for the a- and b-axes, respectively) in the 63–125 μm fraction than in the

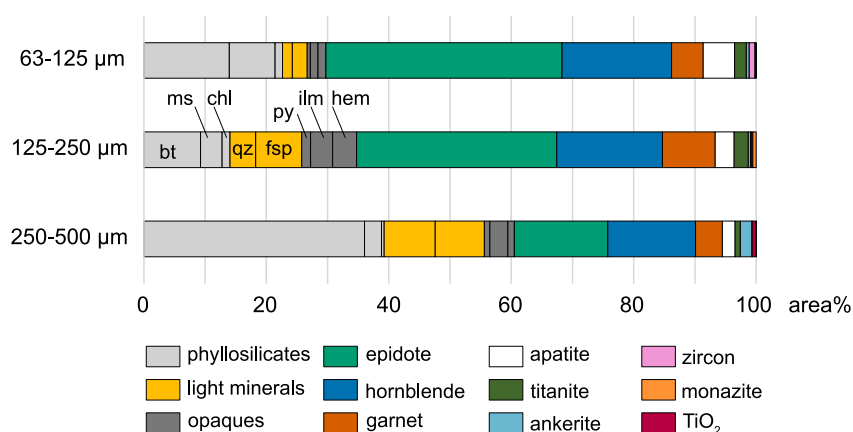


Figure 6. QEMSCAN-derived heavy mineral spectra of the 63–125, 125–250, and 250–500 μm fractions of the Ziller sample (in area %). Mineral abbreviations according to Whitney and Evans (2010); bt = biotite, ms = muscovite, chl = chlorite, qz = quartz, fsp = feldspar, py = pyrite, ilm = ilmenite, hem = hematite. As indicated in the figure, the group of phyllosilicates comprises biotite, muscovite, and chlorite; light minerals comprise quartz and feldspar (often intergrown in rock fragments); and opaques summarize pyrite, ilmenite, and hematite.

125–250 μm fraction (32% for both the a- and b-axes). In the 125–250 μm fraction, the larger standard deviation is caused by the minerals zircon, ankerite, chlorite, and the TiO_2 phase (Figure 8), which all tend to occur as smaller minerals in composite grains.

The measured c-axis lengths (Stutenbecker, 2024g) in the 63–125 and 125–250 μm fractions, respectively, are $84 \pm 11 \mu\text{m}$ and $159 \pm 28 \mu\text{m}$ for apatite, $62 \pm 10 \mu\text{m}$ and $114 \pm 22 \mu\text{m}$ for epidote group minerals, $94 \pm 10 \mu\text{m}$ and $168 \pm 25 \mu\text{m}$ for garnet, $60 \pm 5 \mu\text{m}$ and $96 \pm 18 \mu\text{m}$ for hornblende, $26 \pm 9 \mu\text{m}$ and $41 \pm 10 \mu\text{m}$ for biotite and $67 \pm 11 \mu\text{m}$ and $75 \pm 15 \mu\text{m}$ for zircon. The measured c-axis lengths generally behave linearly to the measured b-axis lengths, but the fit and slope of the linear regression curves differ for different minerals (Figure 9). Apatite, garnet, and zircon show a better fit ($R^2 > 0.8$) than biotite, the epidote group and hornblende. Mean b-to c-axis ratios are 1.1 for apatite, garnet, and zircon, 5.8 for biotite, 1.7 for epidote group minerals, and 1.9 for hornblende.

After applying these metrics in our stepwise scheme (Figure 1) to transform area percent to mass percent (for a stepwise example see Stutenbecker, 2024h), we observe changes in the resulting heavy mineral spectra (Figure 10). The most extreme changes occur for those minerals that are abundant and have large density contrasts, for example, the opaque phases and the phyllosilicates. Compared to their area percentage, the mass percentage of apatites deviates by up to 22%, of ankerite by up to 49%, of epidote group minerals by up to 25%, of garnet by up to 32%, of hornblende by up to 34%, of light minerals by up to 15%, of monazite by 104%, of opaque phases by up to 217%, of phyllosilicates by up to 71%, of the TiO_2 phase by up to 41%, of titanite by up to 98%, and of zircon by up to 78%. We used the achieved mass percentage of apatite and zircon in the heavy mineral concentrate to calculate the apatite and zircon concentrations in the entire sieve fraction (Figure 1) by multiplying with the heavy mineral content (Table 2). This transformation yielded 2,415 ppm and 2,453 ppm of apatite (or

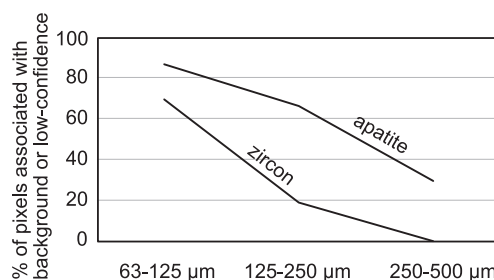


Figure 7. Mineral associations of apatite and zircon in the three considered grain-size fractions show that the frequency of individual apatite and zircon grains decreases with increasing grain size. See Stutenbecker (2024e) for raw data.

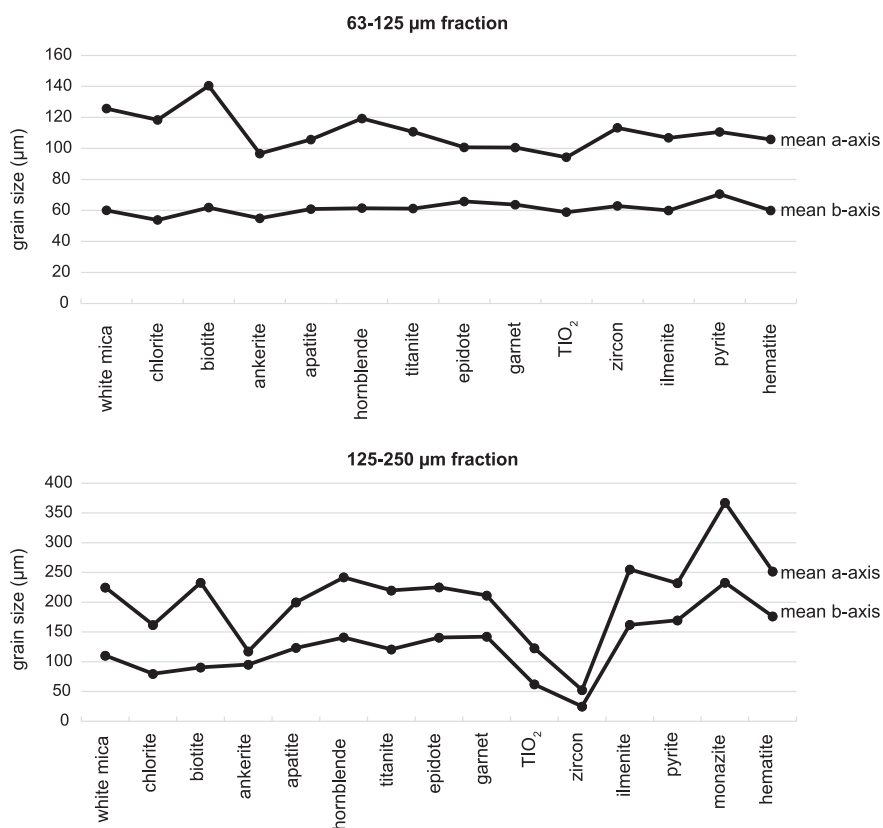


Figure 8. Grain-size metrics from the 63–125 and 125–250 μm fractions of the Ziller sample, derived from measuring the a- and b-axes of all grains contained in the sample.

1,096 ppm and 1,114 ppm of P_2O_5 and 826 and 31 ppm of zircon (or 410 and 15 ppm of Zr) in the 63–125 and 125–250 μm fractions, respectively (Figure 11).

The separation approach yields higher apatite than zircon concentrations and shows that both apatite and zircon contents increase with decreasing grain size (Table 3). The analysis yielded 2,424 ppm apatite and 557 ppm zircon in the 63–125 μm fraction, 1,923 ppm apatite and 129 ppm zircon in the 125–250 μm fraction, and 567 ppm apatite and 67 ppm zircon in the 250–500 μm fraction. These mineral contents would translate to concentrations of 1,048 ppm P_2O_5 and 277 ppm Zr in the 63–125 μm fraction, 873 ppm P_2O_5 and 64 ppm Zr in the 125–250 μm fraction, and 257 ppm P_2O_5 and 33 ppm Zr in the 250–500 μm fraction (Figure 11).

Measured P_2O_5 and Zr contents in the Ziller fractions are 800–3,300 ppm and 104–856 ppm, respectively (Table 4). P_2O_5 and Zr contents increase with decreasing grain size, and the highest concentrations were measured in the <63 μm fraction. Measured P_2O_5 contents are around 1.25 times higher, and Zr contents are approximately two times higher than the values derived from the separation and point-counting approaches (Figure 11).

4. Discussion

The artificial grain mixture experiments show that relative mineral proportions of the same sample, given in mass, number, volume, and area percentage are different. The quartz-magnetite experiment shows that large grain size differences (as simulated by smaller magnetite and larger quartz grains) can cause considerable differences between number percentage and mass percentages. The data further show that area percentage does not necessarily equal volume percentage, which Chayes (1954) showed for rock thin sections but not for unconsolidated grain mixtures. The quartz-biotite sample shows that mass percentage equals volume percentage if the density difference between the grains is not pronounced. Still, the platy shape of mica causes a mismatch of area and volume percentage. Although the grains have complex shapes due to their detrital nature, our approximation of spherical shapes for magnetite and quartz yielded realistic results that matched the known (initial) mass percentages.

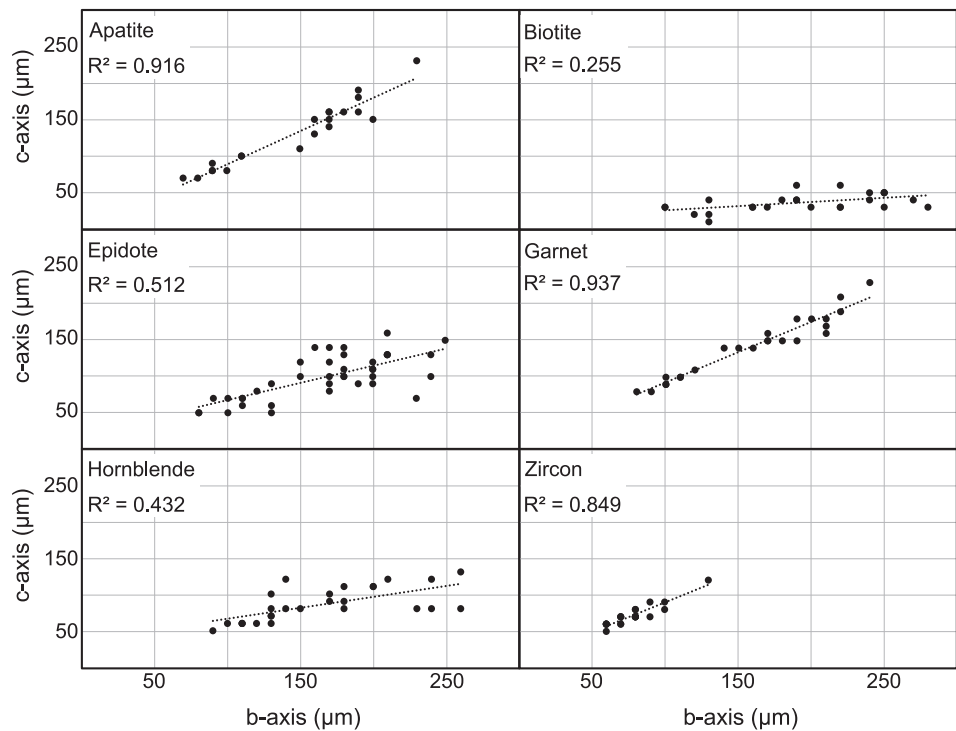


Figure 9. Relationship between the measured b-axis and c-axes of 158 individual grains from the most abundant and easily identifiable minerals apatite ($n = 21$), biotite ($n = 25$), epidote ($n = 39$), garnet ($n = 24$), hornblende ($n = 27$) and zircon ($n = 22$) in the Ziller sediment sample. Note that minerals of both grain-size fractions 63–125 and 125–250 μm were measured, but in the case of zircon, even the coarser grain size fraction did not contain zircon grains larger than ca. 130 μm .

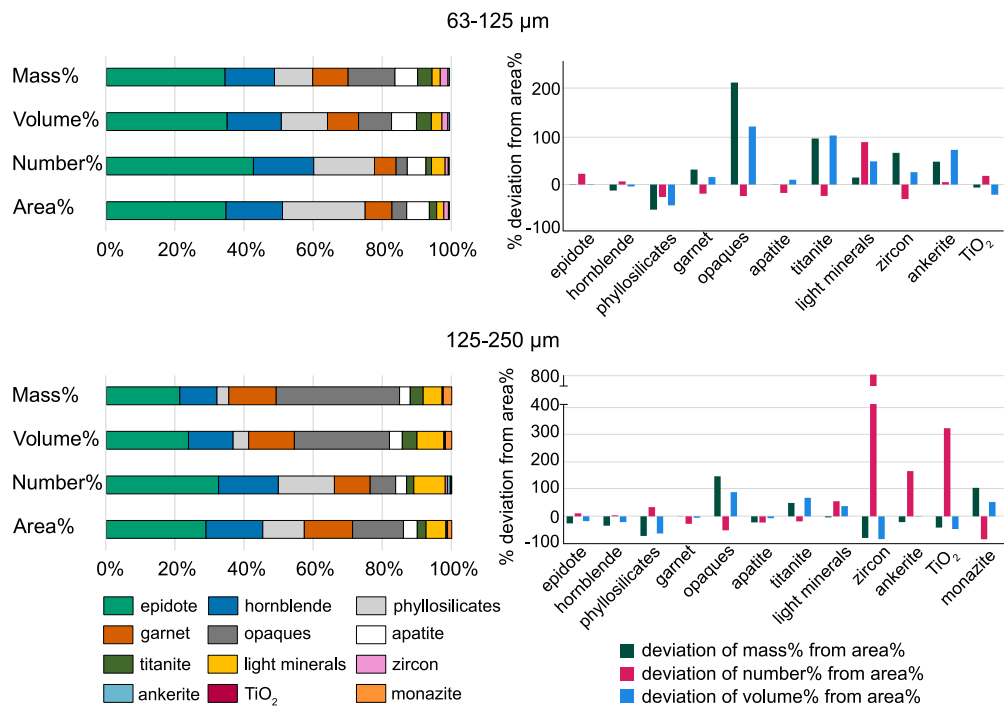


Figure 10. Comparison of area, number, volume, and mass percentage for the different grain-size fractions of the Ziller sample. See Figure 4 for further details. On the right panel, the deviation (in %) of number%, vol%, and mass% from area% is displayed for each mineral. Note that for the 125–250 μm fraction, the y-axis is broken to display a wider range of values.

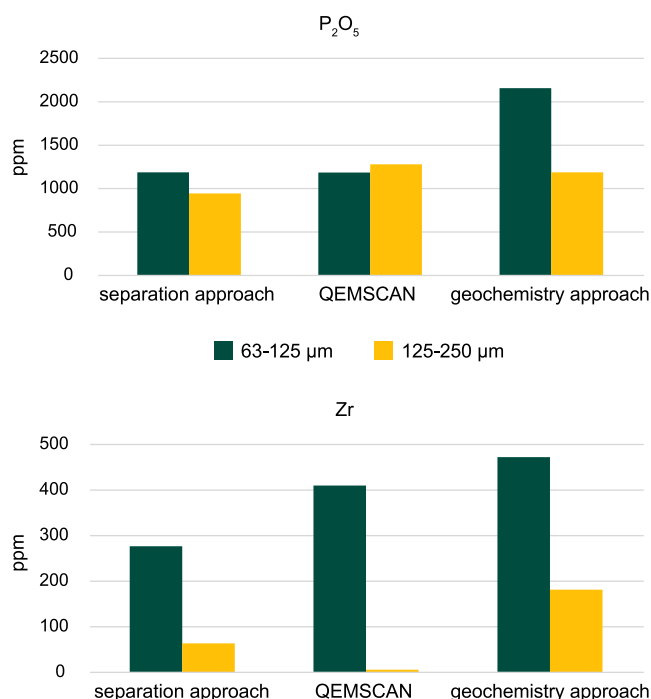


Figure 11. Comparison of P₂O₅ and Zr contents derived from the separation approach (sensu Malusà et al., 2016), the QEMSCAN results (recalculated to mass percent using the proposed method), and the geochemistry approach (sensu Dickinson, 2008). Apatite and zircon contents were recalculated to P₂O₅ and Zr contents by applying atomic/molecular mass factors (see Section 2.9).

Depending on the scope of the study, transformations between these units can be made by measuring or assuming grain-size and shape metrics as well as grain density. Our point-counting results generally faithfully reflect area percentage, as shown by comparing point-counting, image, and grain-size analyses. However, the 1:1:98 quartz-magnetite mixture also shows that point-counting of minerals with very low percentages is associated with high errors (van der Plas & Tobi, 1965), which can influence the calculations. In our case, the minerals were very easy to identify based on color alone, but in natural sediment samples, the error associated with misidentification might be much higher (Dunkl et al., 2020).

Most natural heavy mineral concentrates are a mixture of grains with different densities (from “light” amphibole to “heavy” zircon) and shapes (from near-isometric pyrite to platy micas). This results in potentially significant differences between number, volume, and area percentages. The example of the Ziller sand shows a typical Alpine heavy mineral spectrum with abundant epidote group minerals, amphibole, and mica (Garzanti & Andò, 2007b). The apatite and zircon proportions calculated using the proposed method generally align with the fertility values for granitoid rocks in axial belts measured by Malusà et al. (2016). A comparison between the measured grain sizes and the grain size range expected from the size shift (Resentini et al., 2013, Table 2) shows that the size shift only partially mirrors actual grain size distributions in the heavy mineral concentrate. The MinSorting model, which takes into account hydraulic behavior and not the crystal size distribution in the source rock, predicts significant amounts of zircon (>40%) and apatite (>50%) to occur in the grain-size fractions 250–500 and 500–1,000 μm. However, both QEMSCAN analyses and the separation approach yielded no individual apatite or zircon grains in the 500–1,000 μm fraction and few apatite grains in the 250–500 μm fraction. Instead, P₂O₅ and Zr concentrations are highest in

the <63 μm fraction, which, according to the MinSorting model, should contain less than 5% of all apatite and zircon. Microscopic and QEMSCAN observations confirm that zircon especially does not occur as large individual grains in the grain-size fractions >125 μm. This illustrates that mineral size distributions may not be predominantly controlled by the size shift but rather by the original crystal size in the source rock, and thus should be measured (e.g., through QEMSCAN analysis) to yield reliable mineral distribution data, especially for poorly sorted sediments.

While the geochemistry data of the Ziller sand may scatter depending on the analyzed grain-size fraction, all fractions are chemically similar to more felsic source rock compositions (Figure 12) measured at different locations in or near the Ziller catchment (Finger et al., 1993; Melcher et al., 1996; Wyss, 1993). This supports the idea that felsic granitoid rocks are the dominant source rock in the catchment and that sediment chemistry reflects source rock chemistry in settings with limited chemical weathering (Stutenbecker et al., 2023; von Eynatten et al., 2012). Mineralogical compositions of rocks in the Ziller catchment (Raith, 1970) show that the dominance of epidote and mica can be explained by source rock composition. Thus, the chemical and mineralogical similarity

Table 3
Results of the Separation Approach Using the Ziller Sample

Grain-size fraction	Magnetic fraction [g]	Light fraction [g]	Heavy fraction [g]	Separate between 2.8 and 3.32 g/cm ³ [g]	Of which is apatite (mass%)	Separate >3.32 g/cm ³ [g]	Of which is zircon (mass%)
63–125 μm	6.7168	16.9529	0.1541	0.1375	42	0.0166	80
125–250 μm	16.4039	47.7663	0.3266	0.3100	40	0.0166	50
250–500 μm	33.9036	73.1776	0.5218	0.5080	12	0.0138	52
>500 μm	34.0900	50.7639	0.5636	0.5595	0	0.0041	0

Table 4

Results From Lithium Borate Fusion Coupled With ICP-MS of the Individual Grain-Size Fractions of the Ziller Sample

Grain size fraction (μm)	SiO ₂	Al ₂ O ₃	Fe ₂ O ₃	MgO	CaO	Na ₂ O	K ₂ O	TiO ₂	P ₂ O ₅	MnO	Cr ₂ O ₃	Ba	Sr	Zr	Y	Nb	Sc	LOI
Detection limit	0.01	0.01	0.04	0.01	0.01	0.01	0.01	0.01	0.01	0.01	0.002	5	2	5	3	5	1	
1,000–2,000	71.09	11.85	1.39	1.02	3.92	3.18	3.08	0.19	0.1	0.03	Bdl	805	166	112	13	10	5	4
500–1000	76.53	10.93	1.66	0.7	2.02	3.02	2.7	0.2	0.08	0.04	Bdl	729	149	104	19	6	4	2
250–500	77.22	10.43	2.08	0.77	1.89	2.72	2.41	0.26	0.08	0.04	Bdl	640	145	133	22	6	5	1.9
125–250	76.97	10.77	2.09	0.77	2.1	2.65	2.33	0.29	0.11	0.04	0.002	611	161	182	21	7	6	1.7
63–125	73.65	12.4	2.14	0.77	2.58	2.84	2.7	0.3	0.2	0.04	0.002	638	190	473	28	16	10	1.7
<63	64.17	15.4	2.46	1.17	4.61	3.32	3.71	0.41	0.33	0.05	0.003	807	214	856	48	17	11	4.1

Note. The major element oxides are given in wt%, the trace elements in ppm. Bold values highlight the P₂O₅ and Zr concentrations, which are subsequently used to quantify apatite and zircon concentrations. LOI = loss of ignition, bdl = below detection limit.

between source rock and sand underlines that mineral fertility can be quantified from detrital heavy mineral spectra (Malusà et al., 2016) if changes to the spectrum due to hydraulic sorting can be excluded or corrected.

Malusà et al. (2016) showed that P₂O₅ and Zr contents overestimate the actual apatite and zircon contents in similar sediments because Zr and P may be contained in other phases. In the Ziller case, a similar pattern emerges where geochemical analysis generally yields higher P₂O₅ and Zr contents than the separation and QEMSCAN approaches (Figure 11). Due to the 5- μm -step size in the QEMSCAN analysis, smaller apatite and zircon inclusions could not be detected, but could be additional P₂O₅ and Zr hosts. P₂O₅ could also be hosted in monazite, which was found in low abundances (0.03 and 0.51 area%) in the Ziller sediment. Besides in small zircon inclusions, Zr could be contained in trace amounts in other minerals such as amphibole (Lee et al., 2003), mica (Tischendorf et al., 2001), and ilmenite (Jang & Naslund, 2003; Jia et al., 2022), which are abundant in the Ziller sediment. The P₂O₅ contents calculated via the QEMSCAN approach are generally similar to those calculated via the separation approach (Figure 11). For the 63–125 μm fraction, the fit is almost perfect. This testifies to an effective separation process as supported by the fact that most apatites occur as pure apatite grains and are not frequently intergrown with other phases in this fraction (Figure 7). In the 125–250 μm fraction, there is a mismatch of ca. 300 ppm, which can be explained by the higher proportion of apatites being associated with other phases in this fraction (e.g., epidote group minerals and hornblende, see Stutenbecker (2024e) and a less effective separation. In the 63–125 μm fraction, Zr contents calculated via the QEMSCAN approach are ca. 60 ppm lower

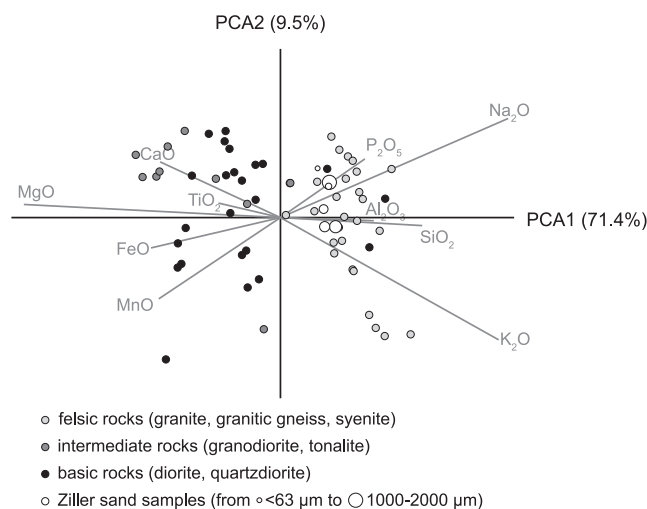


Figure 12. Biplot of principal component analysis showing the similarity of the Ziller sand samples with exposed source rocks in the drainage basin. Major element source rock geochemistry from Wyss (1993), Finger et al. (1993), and Melcher et al. (1996).

than the values from geochemical analysis (Figure 11), suggesting that this amount is hosted in other mineral phases or small zircon inclusions. Zr contents derived from the QEMSCAN approach are about 130 ppm higher than the Zr content calculated via the separation approach. This could be explained by the association of zircons with other phases since only 70% of zircons are present as individual grains (Figure 7), and the separation approach may not separate zircon grains intergrown with other (lighter) phases. In contrast, the Zr contents in the 125–250 μm fraction yielded by the separation approach are higher than those calculated via the QEMSCAN approach. This is somewhat surprising because zircons in this fraction are dominantly associated with other minerals (Figure 7), which would make the separation process less effective. On closer inspection, the zircon concentrate produced through the separation approach contained almost exclusively zircons smaller than 130 μm (Figure 9), which should not be present in this sieve fraction. It is possible that the zircon grains separated from their neighboring minerals during the separation process, and the distribution of zircon grains in the grain size fractions is therefore different compared to the samples prepared for QEMSCAN analysis. Despite these differences, the results from the separation and QEMSCAN approaches are generally within the same order of magnitude, and deviations can be explained considering the detailed information generated through QEMSCAN analysis.

5. Conclusions

This study illustrates that quantitative measures of heavy mineral fertility can be obtained from point-counting detrital minerals in strewn slides, thin sections, or grain mounts. We show that number, area, volume, and mass percentages may vary considerably and that the different grain sizes, shapes, and densities cause these differences. When recording grain sizes and shapes during or after point counting, mineral proportions can be transformed from, for example, area percentage to mass percentage using simplified assumptions and thus can be compared to other “traditional” counting as well as geochemical data sets. The method applied here adds another time-consuming step to heavy mineral studies. However, it works without further magnetic, hydraulic, and chemical separation steps, which may introduce bias (e.g., Sircombe & Stern, 2002), and it works on all mineral species encountered in a sample, not only apatite and zircon. With the advancement of automated mineral identification and quantification techniques, for example, automated mineralogy such as QEMSCAN (Vermeesch et al., 2017) or Raman mapping (Lünsdorf et al., 2019), grain-size and shape metrics will be more readily available. Furthermore, grain-size and shape metrics may add valuable provenance information, such as transport processes and source rocks, as illustrated, for example, in some zircon-based studies (e.g., Augustsson et al., 2018; Gärtner et al., 2013).

Data Availability Statement

The data used in the study are available in the figshare repository under CC BY 4.0 license (Stutenbecker, 2024a, 2024b, 2024c, 2024d, 2024e, 2024f, 2024g, 2024h).

Acknowledgments

We thank Gabriela Schubert and Dirk Scheuven at the Technical University of Darmstadt for their help during sample preparation, and David Chew, one anonymous reviewer and guest editor Alberto Resentini for their constructive and helpful comments. This work was funded through the German Research Foundation (DFG), project number 442580342 within the priority program “4D-MB: Mountain building processes in 4D.” Open Access funding enabled and organized by Projekt DEAL.

References

- Andò, S. (2020). Gravimetric separation of heavy minerals in sediments and rocks. *Minerals*, 10(3), 273. <https://doi.org/10.3390/min10030273>
- Augustsson, C., Voigt, T., Bernhart, K., Kreißler, M., Gaupp, R., Gärtner, A., et al. (2018). Zircon size-age sorting and source-area effect: The German Triassic Buntsandstein Group. *Sedimentary Geology*, 375, 218–231. <https://doi.org/10.1016/j.sedgeo.2017.11.004>
- Bousquet, R., Oberhänsli, R., Schmid, S. M., Berger, A., Wiederkehr, M., Robert, C., et al. (2012). *Metamorphic framework of the Alps*. Commission for the geological map of the world.
- Caracciolo, L. (2020). Sediment generation and sediment routing systems from a quantitative provenance analysis perspective: Review, application and future development. *Earth-Science Reviews*, 209, 103226. <https://doi.org/10.1016/j.earscirev.2020.103226>
- Chayes, F. (1954). The theory of thin-section analysis. *The Journal of Geology*, 62(1), 92–101. <https://doi.org/10.1086/626135>
- Chew, D., O'Sullivan, G., Caracciolo, L., Mark, C., & Tyrrell, S. (2020). Sourcing the sand: Accessory mineral fertility, analytical and other biases in detrital U-Pb provenance analysis. *Earth-Science Reviews*, 202, 103093. <https://doi.org/10.1016/j.earscirev.2020.103093>
- Dickinson, W. R. (2008). Impact of differential zircon fertility of granitoid basement rocks in North America on age populations of detrital zircons and implications for granite petrogenesis. *Earth and Planetary Science Letters*, 275(1–2), 80–92. <https://doi.org/10.1016/j.epsl.2008.08.003>
- Dunkl, I., von Eynatten, H., Andò, S., Lünsdorf, K., Morton, A., Alexander, B., et al. (2020). Comparability of heavy mineral data – The first interlaboratory round robin test. *Earth-Science Reviews*, 210, 103210. <https://doi.org/10.1016/j.earscirev.2020.103210>
- Finger, F., Frasl, G., Haunschmid, B., Lettner, H., von Quadt, A., Schermaier, A., et al. (1993). The Zentralgneise of the Tauern window (Eastern Alps): Insights into an Intra-Alpine Variscan Batholith. In J. F. Raumer & F. Neubauer (Eds.), *Pre-mesozoic geology in the Alps* (pp. 375–391). Springer.
- Folk, R. L., & Ward, W. C. (1957). Brazos river bar: A study in the significance of grain size parameters. *Journal of Sedimentary Petrology*, 27(1), 3–26. <https://doi.org/10.1306/74d70646-2b21-11d7-8648000102c1865d>
- Galehouse, J. S. (1971). Point counting. In R. E. Carver (Ed.), *Procedures in sedimentary petrology* (pp. 385–407). Wiley.

- Gärtner, A., Linnemann, U., Sagawe, A., Hofmann, M., Ullrich, B., & Kleber, A. (2013). Morphology of zircon crystal grains in sediments – Characteristics, classifications, definitions. *Geologica Saxonica*, 59, 65–73.
- Garzanti, E., & Andò, S. (2007). Heavy mineral concentration in modern sands: Implications for provenance interpretation. *Developments in Sedimentology*. In M. A. Mange & D. T. Wright (Eds.), *Heavy minerals in use* (Vol. 58, pp. 517–545). Elsevier. [https://doi.org/10.1016/S0070-4571\(07\)58020-9](https://doi.org/10.1016/S0070-4571(07)58020-9)
- Garzanti, E., & Andò, S. (2007b). Plate tectonics and heavy mineral suites of modern sands. *Developments in Sedimentology*. In M. A. Mange & D. T. Wright (Eds.), *Heavy minerals in use* (Vol. 58, pp. 741–763). Elsevier. [https://doi.org/10.1016/S0070-4571\(07\)58029-5](https://doi.org/10.1016/S0070-4571(07)58029-5)
- Garzanti, E., & Andò, S. (2019). Heavy minerals for junior woodchucks. *Minerals*, 9(3), 148. <https://doi.org/10.3390/min9030148>
- Garzanti, E., Andò, S., & Vezzoli, G. (2008). Settling equivalence of detrital minerals and grain-size dependence of sediment composition. *Earth and Planetary Science Letters*, 273(1–2), 138–151. <https://doi.org/10.1016/j.epsl.2008.06.020>
- Garzanti, E., Andò, S., & Vezzoli, G. (2009). Grain-size dependence of sediment composition and environmental bias in provenance studies. *Earth and Planetary Science Letters*, 277(3–4), 422–432. <https://doi.org/10.1016/j.epsl.2008.11.007>
- Garzanti, E., Resentini, A., Vezzoli, G., Andò, S., Malusà, M. G., & Padoan, M. (2012). Forward compositional modelling of Alpine orogenic sediments. *Sedimentary Geology*, 280, 149–164. <https://doi.org/10.1016/j.sedgeo.2012.03.012>
- Garzanti, E., Resentini, A., Vezzoli, G., Andò, S., Malusà, M. G., Padoan, M., & Paparella, P. (2010). Detrital fingerprints of fossil continental-subduction zones (axial belt provenance, European Alps). *The Journal of Geology*, 118(4), 341–362. <https://doi.org/10.1086/652720>
- GBA (Geologische Bundesanstalt Österreich: Geological Survey of Austria). (2015). GEOFAST maps (1:50000). Map sheet 150 Mayrhofen.
- Gemignani, L., Sun, X., Braun, J., van Gerve, T. D., & Wijbrans, J. R. (2017). A new detrital mica ⁴⁰Ar/³⁹Ar dating approach for provenance and exhumation of the Eastern Alps. *Tectonics*, 36(8), 1521–1537. <https://doi.org/10.1002/2017TC004483>
- Heaman, L., & Parrish, R. (1991). U-Pb geochronology of accessory minerals. In L. Heaman & J. Ludden (Eds.), *Applications of radiogenic isotope systems to problems in Geology* (Vol. 19, pp. 59–102). Mineralogical Association of Canada.
- Jang, Y. D., & Naslund, H. R. (2003). Major and trace element variation in ilmenite in the Skaergaard Intrusion: Petrologic implications. *Chemical Geology*, 193(1–2), 109–125. [https://doi.org/10.1016/S0009-2541\(02\)00224-3](https://doi.org/10.1016/S0009-2541(02)00224-3)
- Jia, L.-H., Mao, Q., Tian, H.-C., Li, L.-X., Qi, L., Wu, S.-T., et al. (2022). High-precision EPMA measurement of trace elements in ilmenite and reference material development. *Journal of Analytical Atomic Spectrometry*, 37(11), 2351–2361. <https://doi.org/10.1039/D2JA00238H>
- Komar, P. D. (2007). The entrainment, transport and sorting of heavy minerals by waves and currents. In M. A. Mange & D. T. Wright (Eds.), *Heavy minerals in use* (Vol. 58, pp. 3–48). Elsevier. [https://doi.org/10.1016/S0070-4571\(07\)58001-5](https://doi.org/10.1016/S0070-4571(07)58001-5)
- Komar, P. D., & Li, Z. (1988). Applications of grain-pivoting and sliding analyses to selective entrainment of gravel and to flow-competence evaluations. *Sedimentology*, 35(4), 681–695. <https://doi.org/10.1111/j.1365-3091.1988.tb01244.x>
- Lammerer, B., & Wegner, M. (1998). Footwall uplift in an orogenic wedge: The Tauern window in the Eastern Alps of Europe. *Tectonophysics*, 285(3–4), 213–230. [https://doi.org/10.1016/s0040-1951\(97\)00272-2](https://doi.org/10.1016/s0040-1951(97)00272-2)
- Lee, J. I., Clift, P. D., Layne, G., Blum, J., & Khan, A. A. (2003). Sediment flux in the modern Indus River traced by the trace element composition of detrital amphibole grains. *Sedimentary Geology*, 160(1–3), 243–257. [https://doi.org/10.1016/S0037-0738\(02\)00378-0](https://doi.org/10.1016/S0037-0738(02)00378-0)
- Lünsdorf, K., Kalies, J., Ahlers, P., Dunkl, L., & von Eynatten, H. (2019). Semi-automated heavy mineral analysis by Raman spectroscopy. *Minerals*, 9(7), 385. <https://doi.org/10.3390/min9070385>
- Malusà, M. G., Resentini, A., & Garzanti, E. (2016). Hydraulic sorting and mineral fertility bias in detrital geochronology. *Gondwana Research*, 31, 1–19. <https://doi.org/10.1016/j.gr.2015.09.002>
- Melcher, F., Prochaska, W., Raith, J. G., & Saini-Eidukat, B. (1996). The metamorphosed molybdenum vein-type deposit of the Alpeiner Scharte, Tyrol (Austria) and its relation to Variscan granitoid. *Mineralium Deposita*, 31(4), 277–289. <https://doi.org/10.1007/bf02280792>
- Moecher, D. P., & Samson, S. D. (2006). Differential zircon fertility of source terranes and natural bias in the detrital zircon record: Implications for sedimentary provenance analysis. *Earth and Planetary Science Letters*, 247(3–4), 252–266. <https://doi.org/10.1016/j.epsl.2006.04.035>
- Morton, A. C., & Hallsworth, C. R. (1999). Processes controlling the composition of heavy mineral assemblages in sandstones. *Sedimentary Geology*, 124(1–4), 3–29. [https://doi.org/10.1016/S0037-0738\(98\)00118-3](https://doi.org/10.1016/S0037-0738(98)00118-3)
- Raith, M. (1970). Schachbrettligoklas in alpidisch metamorphen Gneisen der östlichen Zillertal Alpen (Tirol, Österreich). *Tschermaks Mineralogische und Petrographische Mitteilungen*, 14(2), 141–153. <https://doi.org/10.1007/bf01157312>
- Reid, I., & Frostick, L. E. (1985). Role of settling, entrainment and dispersive equivalence and of interstice trapping in placer formation. *Journal of the Geological Society*, 142(5), 739–746. <https://doi.org/10.1144/gsjgs.142.5.0739>
- Resentini, A., Malusà, M. G., & Garzanti, E. (2013). MinSORTING: An Excel® worksheet for modelling mineral grain-size distribution in sediments, with application to detrital geochronology and provenance studies. *Computers & Geosciences*, 59, 90–97. <https://doi.org/10.1016/j.cageo.2013.05.015>
- Rubey, W. W. (1933). The size distribution of heavy minerals in a water laid sandstone. *Journal of Sedimentary Petrology*, 3, 3–29.
- Schindelin, J., Arganda-Carreras, I., Frise, E., Kaynig, V., Longair, M., Pietzsch, T., et al. (2012). Fiji: An open-source platform for biological-image analysis. *Nature Methods*, 9(7), 676–682. <https://doi.org/10.1038/nmeth.2019>
- Schmid, S. M., Fügenschuh, B., Kissling, E., & Schuster, R. (2004). Tectonic map and overall architecture of the Alpine orogen. *Eclogae Geologicae Helveticae*, 97(1), 93–117. <https://doi.org/10.1007/s00015-004-1113-x>
- Schneider, C. A., Rasband, W. S., & Eliceiri, K. W. (2012). NIH Image to ImageJ: 25 years of image analysis. *Nature Methods*, 9(7), 671–675. <https://doi.org/10.1038/nmeth.2089>
- Sircombe, K. N., & Stern, R. A. (2002). An investigation of artificial biasing in detrital zircon U-Pb geochronology due to magnetic separation in sample preparation. *Geochimica et Cosmochimica Acta*, 66(13), 2379–2397. [https://doi.org/10.1016/S0016-7037\(02\)00839-6](https://doi.org/10.1016/S0016-7037(02)00839-6)
- Sláma, J., & Košler, J. (2012). Effects of sampling and mineral separation on accuracy of detrital zircon studies. *Geochemistry, Geophysics, Geosystems*, 13(5), Q05007. <https://doi.org/10.1029/2012GC004106>
- Stutenbecker, L. (2024a). S1: Area approximation [Dataset]. *Figshare*. <https://doi.org/10.6084/m9.figshare.25399294.v1>
- Stutenbecker, L. (2024b). S2: Grain axes artificial samples [Dataset]. *Figshare*. <https://doi.org/10.6084/m9.figshare.25399342.v1>
- Stutenbecker, L. (2024c). S3: Point-counting results artificial samples [Dataset]. *Figshare*. <https://doi.org/10.6084/m9.figshare.25399516.v1>
- Stutenbecker, L. (2024d). S4: Image analysis (color threshold), artificial samples [Dataset]. *Figshare*. <https://doi.org/10.6084/m9.figshare.25399567.v1>
- Stutenbecker, L. (2024e). S5: QEMSCAN results, Ziller sample [Dataset]. *Figshare*. <https://doi.org/10.6084/m9.figshare.25399579.v1>
- Stutenbecker, L. (2024f). S6: Grain axes Ziller sample [Dataset]. *Figshare*. <https://doi.org/10.6084/m9.figshare.25406977.v1>
- Stutenbecker, L. (2024g). S7: C-axes Ziller samples [Dataset]. *Figshare*. <https://doi.org/10.6084/m9.figshare.25406992.v1>
- Stutenbecker, L. (2024h). S8: Exemplary stepwise calculation of mineral fertility [Dataset]. *Figshare*. <https://doi.org/10.6084/m9.figshare.25406998.v1>

- Stutenbecker, L., Scheuven, D., Hinderer, M., Hornung, J., Petschick, R., Raila, N., & Schwind, E. (2023). Temporal variability of fluvial sand composition: An annual time series from four rivers in SW Germany. *Journal of Geophysical Research: Earth Surface*, *128*(6), e2023JF007138. <https://doi.org/10.1029/2023JF007138>
- Thió-Henestrosa, S., & Martín-Fernandez, J. A. (2006). Detailed guide to CoDaPack: A freeware compositional software. In A. Buccianti, G. Mateu-Figueras, & V. Pawlowsky-Glahn (Eds.), *Compositional data analysis in the geosciences: From theory to Praxis* (Vol. 264(1), pp. 101–118). Geological Society, London, Special Publications. <https://doi.org/10.1144/GSL.SP.2006.264.01.08>
- Tischendorf, G., Förster, H.-J., & Gottesmann, B. (2001). Minor- and trace-element composition of trioctahedral micas: A review. *Mineralogical Magazine*, *65*(2), 249–276. <https://doi.org/10.1180/002646101550244>
- van der Plas, L., & Tobi, A. C. (1965). A chart for judging the reliability of point counting results. *American Journal of Science*, *263*(1), 87–90. <https://doi.org/10.2475/ajs.263.1.87>
- Vermeesch, P., Rittner, M., Petrou, E., Omma, J., Mattinson, C., & Garzanti, E. (2017). High throughput petrochronology and sedimentary provenance analysis by automated phase mapping and LAICPMS. *Geochemistry, Geophysics, Geosystems*, *18*(11), 4096–4109. <https://doi.org/10.1002/2017GC007109>
- Vezzoli, G., Garzanti, E., Limonta, M., Andò, S., & Yang, S. (2016). Erosion patterns in the Changjiang (Yangtze River) catchment revealed by bulk-sample versus single-mineral provenance budgets. *Geomorphology*, *261*, 177–192. <https://doi.org/10.1016/j.geomorph.2016.02.031>
- von Eynatten, H., & Dunkl, I. (2012). Assessing the sediment factory: The role of single grain analysis. *Earth-Science Reviews*, *115*(1–2), 97–120. <https://doi.org/10.1016/j.earscirev.2012.08.001>
- von Eynatten, H., Tolosana-Delgado, R., & Karius, V. (2012). Sediment generation in modern glacial settings: Grain-size and source-rock control on sediment composition. *Sedimentary Geology*, *280*, 80–92. <https://doi.org/10.1016/j.sedgeo.2012.03.008>
- Weltje, G. J., & von Eynatten, H. (2004). Quantitative provenance analysis of sediments: Review and outlook. *Sedimentary Geology*, *171*(1–4), 1–11. <https://doi.org/10.1016/j.sedgeo.2004.05.007>
- Whitney, D. L., & Evans, B. W. (2010). Abbreviations for names of rock-forming minerals. *American Mineralogist*, *95*(1), 185–187. <https://doi.org/10.2138/am.2010.3371>
- Wyss, M. (1993). The migmatite belt at the northern boundary of the Zillertal core of the Tauern Zentralgneisses: A typical intrusive margin. *Schweizerische mineralogische und petrologische Mitteilungen*, *73*, 435–454.
- Zhang, Z., Tyrrell, S., Li, C. A., Daly, J. S., Sun, X., & Li, Q. (2014). Pb isotope compositions of detrital K-feldspar grains in the upper-middle Yangtze River system: Implications for sediment provenance and drainage evolution. *Geochemistry, Geophysics, Geosystems*, *15*(7), 2765–2779. <https://doi.org/10.1002/2014GC005391>